Integrated Plasmonic Infrared Photodetector Based on Colloidal HgTe Quantum Dots

Bingqing Zhu, Mengyu Chen,* Qiang Zhu, Guodong Zhou, Nema M. Abdelazim, Wen Zhou, Stephen V. Kershaw, Andrey L. Rogach, Ni Zhao,* and Hon Ki Tsang*

This paper presents a 2300 nm wavelength photodetector which comprises a spin-deposited colloidal HgTe quantum dot (QD) film on a metal-insulator-metal (MIM) plasmonic waveguide. This photodetector is an integrated device based on the complementary metal-oxide-semiconductor compatible silicon-on-insulator platform. The device employs input and output silicon waveguide grating couplers, and HgTe QDs are used as the infrared photosensing material. Infrared light is coupled to the strongly confined MIM waveguide mode, which shrinks the device footprint and improves the light detection efficiency simultaneously. A room temperature responsivity of 23 mA W^{-1} and a noise-equivalent power of 8.7×10^{-11} W Hz$^{-1/2}$ at 2300 nm wavelength are achieved by the photodetector at 2.14 W mm^{-2} (measured at the input to the plasmonic waveguide) with a device footprint of 15 μm × 0.35 μm. The light intensity–dependent photocurrent, the current noise spectral density, and the 3 dB operation bandwidth are all characterized. The charge transfer properties of the organic HgTe QD films are further analyzed based on field effect transistor measurements.

1. Introduction

Silicon photonic integrated circuits have found applications in optical communication systems,[1] optoelectronic integrated circuits,[2] and optical sensors,[3] and have advanced rapidly in the last two decades. Recently, silicon photonics for optical sensing in the 2–20 μm wavelength range was attracted increasing interest for applications such as spectroscopic sensing,[4] nonlinear optics,[5] bio-sensors,[6] and gas detection.[7] However, further development of integrated photodetectors on silicon waveguides in beyond 2 μm wavelength range suffers from the incompatibility of the available photosensing materials, particularly where the latter may be epitaxial semiconductors.[8] A room temperature operation, complementary metal-oxide-semiconductor (CMOS) compatible chip-scale integrated waveguide photodetector is therefore of much interest for photonic integrated circuits in this wavelength range.[9,10]

The use of plasmonic structures to enhance light absorption as well as light-matter interaction is a widely employed strategy in many light-detection and optical sensing applications.[11,12] It was proved that localized surface plasmon resonances (LSPRs) of metallic nano-structures can enhance the light intensity distribution and absorption in the surrounding media.[13–15] However, the LSPR strategy is not readily applicable to on-chip integrated photonic circuits where light is propagating along the waveguides parallel to the substrate. In contrast with LSPR, the metal-insulator-metal (MIM) wave-guide, guiding surface plasmon polariton (SPP) waves, is an appropriate solution to realize both plasmonic enhancement and chip-scale integration simultaneously. Combining the MIM structures with functional materials to achieve electro-optic modulation[16,17] and photodetection[18,19] in the near-IR range has already been demonstrated. Application of this concept may also be promising for integrated photodetectors in the longer wavelength range. The MIM structure offers small effective mode field area, for device dimensions in the deep-subwavelength range rather than scaling up with wavelength, which greatly shrinks the device footprint and thickness. Moving to longer wavelengths also allows the SPP mode propagation loss to be lower.[20]

The choice of the photosensing material is another critical issue in the photodetector design. Commercial narrow-band mid-IR photodetection semiconductors such as HgCdTe[21] and InSb[22] require low-temperature operation.[23,24] 2D materials such as graphene[25] and black phosphorus[26] have attracted interest as possible alternatives. However, graphene is difficult to integrate and pattern on large-scale silicon photonic integrated circuits, and black phosphorous to date is only available by mechanical exfoliation and can become degraded by oxidation.[27] Colloidal HgTe quantum dots (QDs), with a controllable response spectrum that spans almost the entire

Dr. B. Zhu, Dr. M. Chen, Dr. Q. Zhu, G. Zhou, Dr. W. Zhou,
Prof. N. Zhao, Prof. H. K. Tsang
Department of Electronic Engineering
The Chinese University of Hong Kong
Shatin, New Territories, 999077 Hong Kong SAR, China
E-mail: mengyuchen@cuhk.edu.hk; nzhao@cuhk.edu.hk;
hktsang@ee.cuhk.edu.hk
Dr. N. M. Abdelazim, Dr. S. V. Kershaw, Prof. A. L. Rogach
Department of Materials Science and Engineering and Centre
for Functional Photonics (CFP)
City University of Hong Kong
Kowloon, 999077 Hong Kong SAR, China

**ADVANCED
SCIENCE NEWS**
www.advancedsciencenews.com

**ADVANCED
MATERIALS
TECHNOLOGIES**
www.advmattechnol.de

near- to mid-IR range,[28] have emerged as an attractive candidate for IR light detection.[29–32] Such QDs, synthesized and stabilized in solution phase with various ligands,[33–36] can be easily integrated with the standard silicon-on-insulator (SOI) platform due to the solution processability and low-temperature deposition methods that are applicable. Moreover, the photocarrier generation and hopping mechanism under the quantum confinement condition[37] reduces the dark current and noise level of the HgTe QDs–based photodetectors and potentially offers a competitive sensitivity at room temperature in beyond 2 µm range.

In this work, we explore the chip-scale miniaturization and CMOS compatible fabrication of the HgTe QD–based photodetector beyond 2 µm. First, a plasmonic-silicon hybrid waveguide system, composed of an MIM waveguide with silicon input and output couplers, was designed and fabricated to operate in the specific wavelength range. Second, a layer of colloidal HgTe QDs with matched photoresponse wavelength was spin-deposited onto the plasmonic-silicon hybrid waveguide for photoconductive detection. In this device, the detected light was transferred and monitored by the strongly confined MIM waveguide mode, which increased the light detection efficiency and shrank the device footprint simultaneously. The experimental results of the optical transmission characteristics of this photodetection system were in good agreement with the simulation results. A room temperature responsivity of 23 mA W^{-1} and a noise-equivalent power (NEP) of 8.7×10^{-11} W Hz$^{-1/2}$ at 2300 nm wavelength were achieved under a light illumination level of 2.14 W mm^{-2} with a device footprint of 15 µm × 0.35 µm. The light intensity–dependent photocurrent was measured in devices with different MIM waveguide lengths, to investigate the photogeneration and recombination mechanism. The current noise spectral density and the 3 dB operation bandwidth of the devices were characterized as practical photodetectors. Field effect transistor (FET) measurements further revealed the charge transfer properties in HgTe QD films and the photodetection properties.

2. Result and Discussion

2.1. Device Design and Fabrication

The schematic of the on-chip plasmonic photodetection system is depicted in **Figure 1**a. It composes of three main parts, the input, and output silicon grating couplers, a pair of silicon-to-SPP mode converters and the central MIM waveguide filled with a layer of spin-deposited HgTe QDs which works as the light detection medium. The input and output grating couplers are apodized focusing nanostructured silicon grating couplers[38] with the peak operation wavelength around 2300 nm after HgTe QD coating (i.e., taking into account the modified local permittivity, will be discussed later). The couplers are located at the beginning and end of this system, respectively, and are connected to a pair of silicon-to-SPP mode converters through two single-mode silicon strip waveguides. Each silicon-to-SPP mode converter consists of a silicon strip-to-slot structure and a reversed taper-funnel structure,[39] as illustrated in Figure 1a. Between the pair of silicon-to-SPP converters, two horizontally located gold pads (separated by a gap of a few hundred nanometers) form the MIM waveguide for SPP wave propagation—the principal component of the system. To form the photoactive layer, HgTe QDs were directly deposited on top of the entire plasmonic-silicon hybrid waveguide system described above and filled into the gap of MIM waveguide. The cross-section AA' of the MIM waveguide after QD deposition is illustrated in the inset of Figure 1a (note that for clear illustration of the plasmonic-silicon hybrid waveguide system, we do not depict the HgTe QDs in the main picture of Figure 1a). When connected to an external bias voltage, the gold pads forming the MIM waveguide also function as the electrodes of this photoconductive detector.

The photodetection process of the system can be described as follows. The incident light from a tunable continuous-wave laser with central wavelength 2300 nm was focused onto a ZrF$_4$ fiber through a lens. Then, the light in the fiber mode was coupled to the on-chip system through an apodized
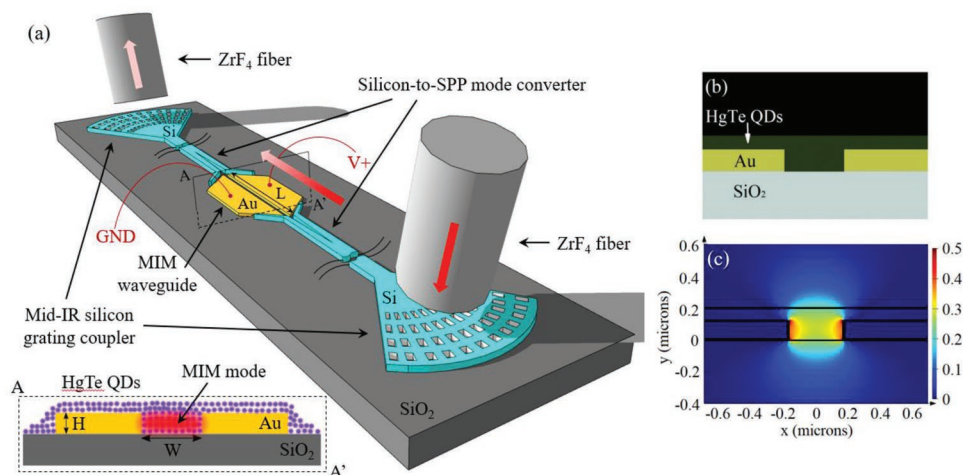

Figure 1. a) The schematic of the plasmonic-silicon hybrid waveguide system. The red arrows show the light propagation direction. Inset: the cross-section AA' of the MIM waveguide with HgTe QD coating. The purple dots represent the HgTe QDs. b) The simulation schematic of the cross-section of HgTe QD-loaded MIM waveguide. c) The simulated electric field distribution of the above MIM mode.

**ADVANCED
SCIENCE NEWS**
www.advancedsciencenews.com

**ADVANCED
MATERIALS
TECHNOLOGIES**
www.advmattechnol.de

grating coupler with a selected transverse electric (TE) polarization. The light propagated along the silicon strip waveguide to the silicon-to-SPP mode converter. During the mode conversion, the silicon strip mode is first converted into a silicon slot mode, and then the slot mode is coupled to the MIM mode by a slot–slot mode effective index matching scheme at the MIM waveguide. The MIM mode here can be understood as a coupled mode of two SPP waves which are generated at two parallel and neighboring metal/HgTe QD surfaces. The SPP waves can only be excited by the light with the electric field oscillation perpendicular to the metal-dielectric surface. That is why the TE polarization was selected for the incident light coupling into the system.

The MIM mode distribution in the HgTe QD–loaded MIM waveguide structure was simulated using the Lumerical MODE Solutions[40] package based on the permittivity of the HgTe QD layer experimentally measured by the ellipsometry technique (Figure S1 in the Supporting Information). Figure 1b is the cross-section of the simulation model of the HgTe QD–loaded MIM waveguide and Figure 1c is the simulated electric field distribution of the MIM mode. The simulation shows clearly that the MIM mode is strongly confined within the slot region which is attributed to the significant permittivity difference between the HgTe QDs and the gold structures. Accordingly, the SPP waves propagating along the MIM waveguide were absorbed by the HgTe QDs in the slot region. With the external bias on the MIM waveguide, the photogenerated electron–hole pairs in the HgTe QDs were efficiently separated and collected by the electrodes. The extracted photocurrent was used to record the light power passing through the MIM waveguide. At the end of the MIM waveguide, the residual SPP waves were back-converted into the silicon waveguide and coupled out of the on-chip system with similar mode converter and grating coupler arrangements to the input side of the device. The output power was monitored by an optical spectrum analyzer (OSA).

It is worth mentioning that the MIM waveguide, which works as the photoconductive electrodes at the same time, provides an almost 100% overlap between the optical mode and the electric field, which is highly desirable in efficient optoelectronic devices, especially in optical modulators[41] and photodetectors.[42] Moreover, since the two gold pads forming the MIM waveguide were closely placed with a gap of a few hundred nanometers, only a small voltage was needed to create a large electric field in the slot region. In this sense, the device is more energy-efficient compared to free-space devices which normally have micrometer range electrode spacings. Note also that the light absorbed by the HgTe QDs covering the grating couplers cannot contribute to the photocurrent because the distance between the grating couplers and the MIM waveguide is about 200 µm, which is much longer than the average diffusion length of the photocarriers in the QD films. The evanescent field leaking around the silicon waveguide, although it may be absorbed by the HgTe QD layer, is obviously much weaker than the strongly confined MIM mode field in the slot region. Thus, the photocurrent observed in this system is mainly attributed to the absorption of the SPP waves within the MIM waveguide.

After the simulation, the on-chip plasmonic-silicon hybrid photodetection system was fabricated on a standard SOI wafer with 250 nm top silicon and 3 µm buried oxide. Two steps of electron-beam lithography (EBL) were employed to build the plasmonic-silicon hybrid waveguide system. The silicon grating couplers, strip waveguides, and silicon-to-SPP mode converters were created in the first EBL step followed by a deep reactive-ion etching (DRIE) process. The MIM waveguide and all other metal parts were fabricated in the second EBL step under careful alignment with the preceding silicon counterparts, followed by metal deposition and lift-off. Two MIM waveguides with different SPP waveguiding lengths (7.5 and 15 µm) were made side by side on the same chip for comparison. The scanning electron microscope (SEM) image of the two devices is shown in **Figure 2**a. The magnified SEM images of the silicon grating coupler and two MIM waveguides are illustrated in Figure 2c–e, respectively. In both cases, the MIM waveguides and the silicon-to-SPP mode converters are mutually well-aligned, as expected. For both MIM waveguides, the width of the slot is kept around 350 nm, and the strip width of the silicon waveguide is 650 nm. After validating the performance of this plasmonic-silicon hybrid waveguide through the optical transmission test, colloidal HgTe QDs were directly spin-coated onto the entire chip to form the photoactive layer. The HgTe QDs were synthesized by an aprotic solvent/gas injection method,[31,35] and after solvent and ligand exchange, capped by dodecanethiol (DDT) ligands and re-dispersed in toluene. The average size of the particles is about 5–6 nm, with the photoluminescence peak located at 2100 nm. According to our previous study using the similar QD size,[31] the solid QD film can exhibit good sensitivity up to 2200 nm. We therefore designed the working wavelength of the grating coupler as 2200 nm and used a QD refractive index estimated from the ellipsometry measurement. After device fabrication, we found that the working wavelength of the grating coupler is shifted from 2200 to 2300 nm, suggesting that the actual QD cladding index is higher than our estimation. After layer-by-layer spin-deposition and further ligand exchange "in film" of DDT to 2-mercaptopropionic acid (MPA), the HgTe QDs became closely packed and filled the MIM waveguide slot region with a layer thickness around 200 nm. Such thickness is optimized by balancing the optical loss in the grating coupler (thinner films are preferred) and the light absorption and conductivity of the QD film (thicker films are preferred). Note also that the film quality becomes poor when there are too many iterations of the spin-coating and ligand exchange processes. Figure 2b shows the microscopic image of the plasmonic-silicon hybrid waveguide system after the HgTe QD deposition. The HgTe QD layer is smooth and semi-transparent under visible light, which allows for optical alignment between the fiber and the grating coupler during the device characterization.

2.2. Optical Transmission Properties

Typical optical transmission loss spectra of the plasmonic-silicon waveguides clad with the HgTe QD layer are shown in **Figure 3**. The transmission peak wavelength of 2300 nm is clearly observed in both samples with the different MIM waveguide lengths. By comparing the transmission losses between the two samples, the MIM mode propagation loss is estimated to be 0.9 dB µm^{-1} at 2300 nm, indicating that 78.5% and 95.5%
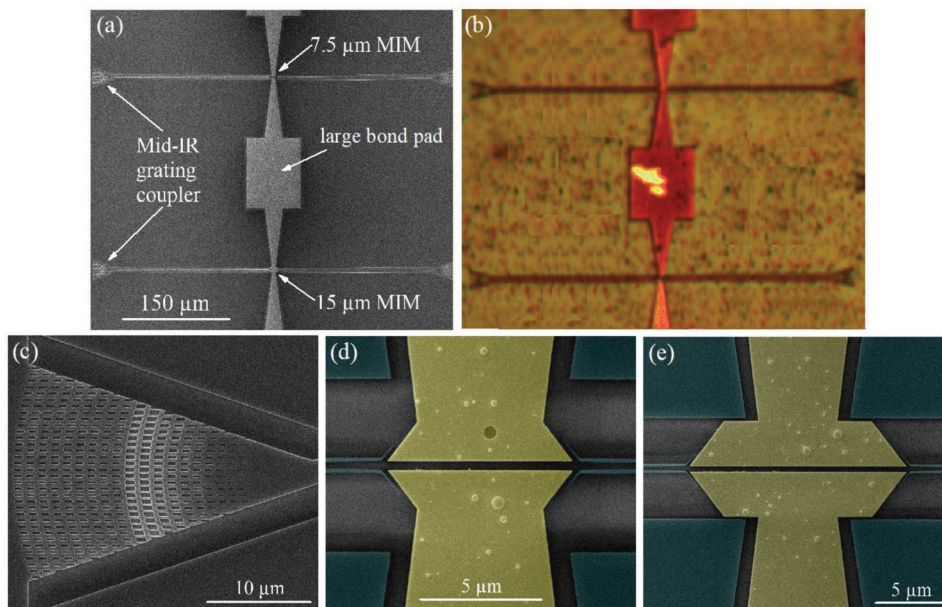
Figure 2. a) The SEM image of the device before spin-coating the HgTe QDs. b) The microscopic picture of the same device after spin-coating HgTe QDs. c) The SEM image of the TE apodized silicon grating coupler. (d) and (e) are further magnified SEM images of the light detection region for the 7.5 and 15 µm devices, respectively.

of the input power is absorbed in the 7.5 and 15 µm length MIM waveguides, respectively. These results agree reasonably well with the simulation result of MODE Solutions. From the simulation, the MIM mode propagation loss including loss from the HgTe QD cladding is 0.78 dB µm^{-1} at 2300 nm, which confirms that the performance of the fabricated HgTe QD–loaded plasmonic-silicon waveguides is close to the theoretical device model. We also simulate the MIM mode loss from metal is 0.44 dB µm^{-1}, and the effective absorption of the HgTe QDs is 0.34 dB µm^{-1}. More than half of the input power loses in metal instead of HgTe QDs.

2.3. Photodetection Characterization

For photodetection applications, the current–voltage photo-response of the devices with different MIM waveguide lengths was characterized under different input light power. As shown
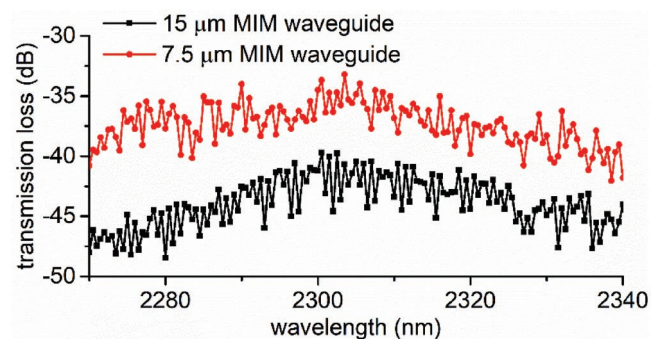

Figure 3. The optical transmission loss spectra of the two MIM waveguides with different lengths, with the HgTe QD cladding present.

in **Figure** 4a,b, the changes of the current in both devices clearly reflect the changes of the input light power, ranging from less than 1 µW to over 100 µW. The illustrated input power is defined by the light power entering the MIM waveguides (detailed calculation is provided in the Supporting Information). The optical power that was lost in the silicon grating coupler and the silicon-to-SPP mode converter before entering the MIM waveguide has been excluded from the photoresponse calculation since it is irrelevant to the photocurrent generation mechanism. At a bias voltage of 2 V, the dark current of the 15 µm length MIM waveguide was 70 nA, which was twice as much as the 7.5 µm device. Since the photoconductor is basically a photosensitive resistor, the dark current doubling can be understood easily by considering two identical resistors connected in parallel, resulting in a halved total resistance.

The input light power–dependent photocurrent and responsivity are calculated for both devices, as shown in Figure 4c,d. Under 0.54 µW input light power, the responsivity of the photodetector with the 15 µm MIM waveguide reaches 23 mA W^{-1} at 2 V bias, while it is 17.5 mA W^{-1} for the 7.5 µm MIM waveguide device. The 15 µm photodetector has a slightly higher responsivity because more light power is absorbed by a longer waveguide. However, most of the power in the SPP waveguide is lost in the first few microns. Doubling the waveguide length results in 31% increment in the responsivity but 100% increase in the dark current. If the length is further increased, one can expect that the further increment of the responsivity will be small while the increase of the dark current will be significant as it scales with the channel length. With MODE Solutions, we calculate the MIM mode effective area in our devices to be around 0.25 µm^2. That is, 0.54 µW light input power corresponds to an average light intensity of 2.14 W mm^{-2}, which is over two orders of magnitude higher than the highest light illumination
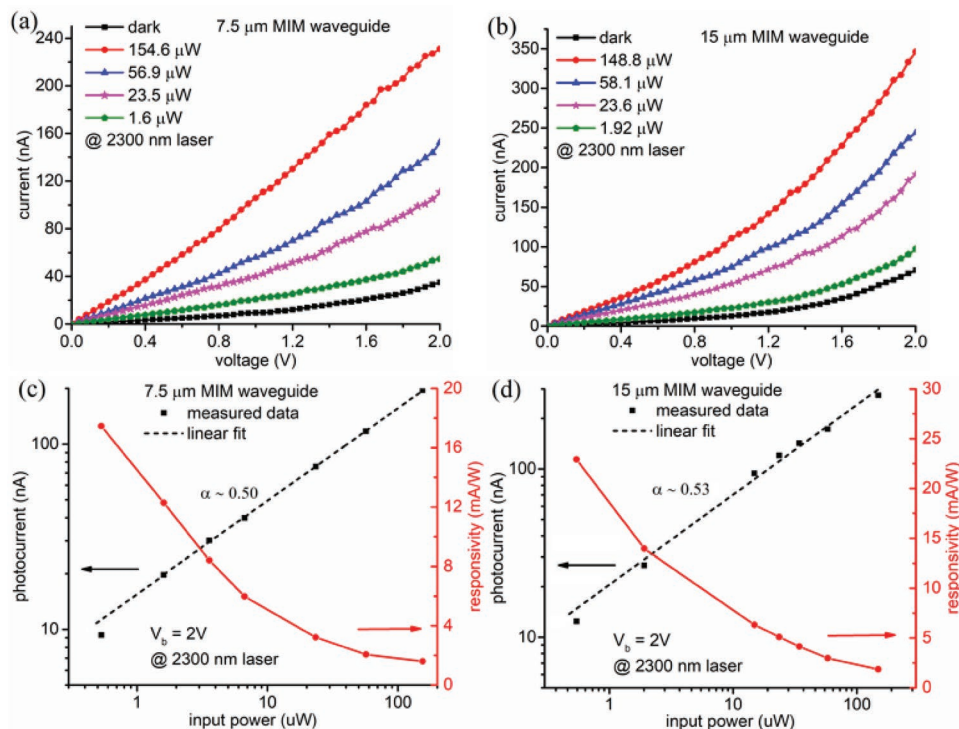
ADVANCED
SCIENCE NEWS
www.advancedsciencenews.com

ADVANCED
MATERIALS
TECHNOLOGIES
www.advmattechnol.de

Figure 4. I–V curves under different light input power for the a) 7.5 µm device and b) 15 µm device, respectively. Black dots and dotted line in c) and d) show the measured and linear fitted data of the net photocurrent versus input light power under a 2 V bias voltage, both in logarithm scale. The red solid line shows the responsivity for a range of light powers under 2 V bias voltage. (c) and (d) represent the 7.5 µm device and 15 µm device, respectively. The input light wavelength was fixed at 2300 nm in all measurements.

level mentioned in the literature for free space applications.[43] We note that a higher responsivity may be achieved with lower light input power. However, under the input power of 0.54 µW (−33 dBm), the output power from this integrated waveguide system is −75 dBm, almost reaching the lowest detection limit of our OSA.

The reduced responsivity at increased input light power indicates the increasing dominance of bimolecular recombination over trap-assisted recombination; the latter typically provides much higher responsivity due to photoconductive gain.[32,43,44] That can be further illustrated by analyzing the power-law dependence of the photocurrent (I_{ph}) on the light intensity (I), i.e., $I_{ph} \propto I^\alpha$. As shown in Figure 4c,d, the gradient of the linear fitted slope, α, for the 7.5 and 15 µm photodetector were both close to 0.5 in the above 1 µW input power region. That indicates that the dominant loss mechanism of the photogenerated carriers is bimolecular recombination,[44] which normally

happens under high illumination levels in such photoconductive devices. For input power lower than 1 µW, the photocurrent points both fall below the $\alpha = 0.5$ fitting lines, which means that the fitting slope increases to more than 0.5, and trap-assisted recombination also plays a role in this region.

In the following, we choose the 15 µm length photodetector to characterize the noise level and response speed as that device had better responsivity. **Figure 5**a shows the current noise spectral density of the 15 µm length photodetector. At low frequency, the current noise density follows a 1/f trend. This 1/f noise also occurs in other QD-based photodetectors, suggesting the noise characteristics are dominated by the nanocrystalline nature of the QD films.[45,46] Based on the current noise spectral density, the NEP can be evaluated using NEP = i_n/R,[47] where R is the responsivity and i_n is the current noise density. With the current noise at 1 kHz and the highest responsivity measured, the room temperature NEP
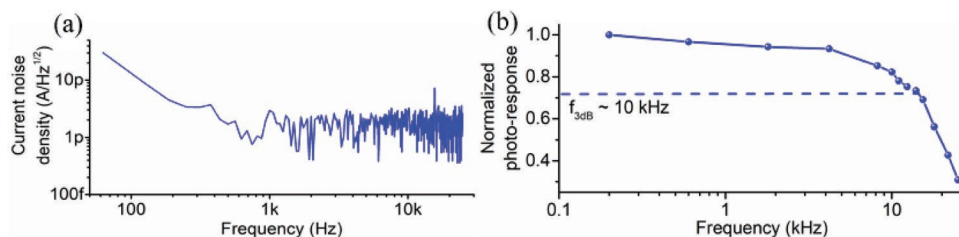

Figure 5. a) The current noise density of the 15 µm device. b) The normalized photoresponse versus the modulation frequency of the 15 µm device at 1620 nm light wavelength under 1.6 V bias voltage. The 3 dB bandwidth is located at 10 kHz.

**ADVANCED
SCIENCE NEWS**

www.advancedsciencenews.com

**ADVANCED
MATERIALS
TECHNOLOGIES**

www.advmattechnol.de

and detectivity D^* of our photodetector with the 15 µm length MIM waveguide is calculated to be 8.7×10^{-11} W Hz$^{-1/2}$ and 3.2×10^6 cm Hz$^{1/2}$ W^{-1} (Jones). Note that the detectivity of waveguide-integrated photodetectors is normally much lower than that of free-space photodetectors due to the much smaller active area of the former. The application scenarios of these two types of photodetectors are also different. The 3 dB bandwidth was measured by recording the photoresponse as a function of the light modulation frequency for the same device. As shown in Figure 5b, the 3 dB bandwidth of the 15 µm length photodetector exceeds 10 kHz.

We compare the performance of our devices to other representative published photodetectors based on integrated waveguiding system in Table S1 in the Supporting information. As shown in the table, the NEP and lowest input power are the major parameters for evaluating the sensitivity of the integrated photodetectors. If we compare our device to the graphene or black phosphorus–based integrated infrared photodetectors, our device shows advantage in sensitivity with low NEP. That is consistent with the observation in free-pace photodetectors— the QD-based photodetectors normally have lower dark current compared with the devices based on 2D materials. To the best of our knowledge, our photodetector is the first QD waveguide-integrated device for beyond 2 µm photodetection.

2.4. FET Measurements

To further investigate the charge transport properties of the HgTe QD films in our devices, a bottom-contact bottom-gate FET structure was fabricated. With the same toluene-based HgTe QDs and the same deposition method as described above, we fabricated a layer of HgTe QDs on a doped silicon wafer (used as the gate electrode) covered with a 300 nm thermally grown SiO$_2$ layer (used as the gate dielectric) and a pair of pre-patterned gold electrodes (used as source-drain electrodes). The device structure and the typical transfer curves of the FET are, respectively, shown in Figures S2 and S3 in the Supporting Information. Compared to the previously reported aqueous-phase HgTe QD–based FETs with the same device structure,[31] the ambipolar property of the organic-phase (toluene) HgTe QD device is more pronounced. The typical hole and electron mobility values of the organic-phase HgTe QD FET are calculated to be $\mu_h \approx 4 \times 10^{-4}$ cm^2 V^{-1} s^{-1} and $\mu_e \approx 1.37 \times 10^{-4}$ cm^2 V^{-1} s^{-1}, respectively.

With the 3 dB bandwidth measured in Figure 5b, the average lifetime of the trap states in our devices can be estimated to be 16 µs according to $\tau_c = 1/(2\pi f_{3dB})$.[47] Therefore, the average photoconductive gain in our devices can be evaluated with $G = \tau_c(1/\tau_{th} + 1/\tau_{te})$, where τ_{th} and τ_{te} are the transit time required for the photogenerated hole and electron to drift to electrodes under a given bias voltage.[44] τ_{th} and τ_{te} can be, respectively, calculated with $\tau_{th} = L^2/(V \cdot \mu_h)$ and $\tau_{te} = L^2/(V \cdot \mu_h)$, where L is the electrode spacing (350 nm) and V is the applied voltage (1.6 V) in our case. Therefore, the average photoconductive gain in our devices is evaluated to be around 11.3. Note that this gain value is estimated for a trap-assisted recombination process, which typically occurs at low light intensity. In our actual measurement (Figure 4), a high light intensity of

2.14 W mm^{-2} was used due to the detection limit of our OSA; in this case the photodetection is dominated by bimolecular recombination and the gain may not exceed 1.

3. Conclusions

In summary, we have demonstrated an on-chip IR photodetector system where the photosensing HgTe QD medium was integrated with silicon-plasmonic waveguides. A room temperature responsivity of 23 mA W^{-1} and an NEP of 8.7×10^{-11} W Hz$^{-1/2}$ at 2300 nm wavelength were achieved with a device footprint of only 15 µm × 0.35 µm under a 2.14 W mm^{-2} illumination level. With its good compatibility with silicon technology and compact device structure, this photodetector design may have promising applications in on-chip real-time light signal monitoring in integrated photonics in beyond 2 µm wavelength range. The design and fabrication methods of integrating plasmonics, functional materials, and silicon photonics are demonstrated in this study and the related device characterizations shed some light on the future prospects for integrated near- and mid-IR photonic circuits.

4. Experimental Section

Plasmonic-Silicon Hybrid Waveguide Fabrication: The device was fabricated on an SOI wafer with 250 nm top silicon and 3 µm buried oxide (from SOITEC). Two steps of EBL (ELS-7800 from ELIONIX Company) were employed, one step of dry etching and one step of metal deposition to build this device. The first EBL layer was used to build silicon structures. Before the first EBL layer, the positive E-beam resist (ZEP-520A, from ZEON) was spin-coated onto the SOI substrate at 3500 rpm for 1 min, and the resist thickness was around 450 nm. Then, the sample was placed onto a hot plate for a pre-bake at 180 °C for 3 min. After writing, the sample was developed with the developer (ZED-N50, from MicroChem) at 0 °C for 1 min and rinsed in methyl isobutyl ketone (MIBK, from MicroChem) and isopropyl alcohol (IPA) stirred solution (9:1) at room temperature for 30 s. After development, the sample was post-baked at 120 °C for 3 min. Then, the sample went through a silicon fully etched process by using a C$_4$F$_8$ and SF$_6$ gas mixture (gas volume ratio C$_4$F$_8$:SF$_6$ = 2:3) with the DRIE machine (Oxford Plasma 100 Dual Chamber). In these steps, the silicon grating couplers, the silicon waveguides, and the silicon parts of the silicon-to-SPP mode converters were created. The plasmonic waveguide was fabricated with the second EBL writing sequence. A step of O$_2$ plasma cleaning was used to remove the residual resist on the sample by using a plasma machine (Oxford Plasma Lab 80 Etcher). After that, another positive E-beam resist, PMMA 950 A7 (from MicroChem), was spin-coated onto the SOI substrate at 3500 rpm for 1 min, and the resulting resist thickness was around 650 nm. The sample was placed into an oven for a pre-bake at 180 °C for 3 min. During the second EBL writing, the windows for the plasmonic waveguide and large electrical bond pads were opened. Note that extremely careful alignment between features from the previous stage and this step was required since the fabrication tolerance was normally within 50 nm in both the x- and y-directions in the device plane. After writing, the sample was developed with a developer (MIBK:IPA = 1:3) at 0 °C for 1 min 30 s and rinsed in IPA at room temperature for 45 s. Then, metal layers (3 nm Cr and 120 nm Au) were deposited onto the sample by using a sputtering machine (Anatech Hummer XII Magnetron Sputtering System). The last step in the process was metal lift-off by immersing in acetone for half an hour.

HgTe QD Synthesis and Film Deposition: The HgTe QDs were synthesized by room temperature growth in dimethyl sulfoxide with

2-furanmethanethiol (FMT) ligands, and then transferred into organic solvents (tetrachloroethylene for spectroscopy, and toluene for device fabrication) with the FMT replaced with DDT ligands. After ligand exchange, the solution was purified several times to remove residual traces of the synthesis solvent and precursors and then to reduce the DDT concentration to the minimum level required for colloid stabilization in the organic solvent. For device fabrication, the QDs were re-dispersed in toluene in the final purification step because the viscosity and volatility of toluene were more suitable for spin-coating deposition. After 5 min O_2 plasma treatment, 70 µL HgTe QD solution was directly dropped onto the prepared silicon-plasmonic waveguide chips, and then spin-dried at 1000 rpm for 100 s. Next, 100 µL MPA:acetonitrile (ACN) = 2:100 (volume ratio) solution was dropped over the whole QD film and left static for 15 s for ligand exchange to occur, and then spin-dried at 1000 rpm for 100 s. During the spinning, 1000 µL ACN solution was quickly dropped onto the sample to rinse out the residual MPA ligands on the surface. After 10 min 60 °C baking on a hotplate, the sample was ready for a second round of HgTe QD spin-deposition and a repeated ligand exchange process. After four rounds of deposition in this manner, the thickness of QD layer reached about 200 nm.

Characterization: The SEM imaging was carried out on an FEI Quanta 400 FEG microscope. For optical transmission measurements, the input light provided by an IPG CLT-2500 tunable continuous-wave laser, and the light wavelength was tuned from 2260 to 2340 nm with fixed output power. The free space light from the laser was focused to a ZrF_4 fiber core through a focusing lens. After light transmission in the silicon-plasmonic waveguide system, the residual light coupling out of the on-chip system was re-collected at another ZrF_4 fiber and its wavelength and power were monitored by a Yokogawa AQ6375 optical spectrum analyzer. The current–voltage properties under different light input powers were characterized with the same light source and output monitor used in the optical transmission measurement, with the laser light power tuned from 20 to −4 dBm, again with the wavelength fixed at 2300 nm. The photocurrent was recorded by a Keithley 2400 Source Meter with electrical contact probes. The voltage was scanned from 0 to +2 V. The noise current spectral density was measured by an SR760 FFT spectrum analyzer (Stanford Research Systems) with devices sealed in a metal shielding box. The chip was wire-bonded to a chip carrier with a battery-based voltage supply. For 3 dB bandwidth measurements, an SR830 DSP lock-in amplifier (Stanford Research Systems) based set-up was used. The near-IR light source used was an L-band Santec TSL-510 laser. The laser light was externally modulated by the same lock-in amplifier. The applied bias voltage was also provided by a battery. The transfer characteristics of the FET devices were measured with a Keithley 2612 Source Meter with a pulse mode scan (pulse width = 100 ms, sampling interval = 1–2 s).

Supporting Information

Supporting Information is available from the Wiley Online Library or from the author.

Conflict of Interest

The authors declare no conflict of interest.

[1] V. R. Almeida, C. A. Barrios, R. R. Panepucci, M. Lipson, *Nature* **2004**, *431*, 1081.

[2] Q. Xu, B. Schmidt, S. Pradhan, M. Lipson, *Nature* **2005**, *435*, 325.

[3] K. De Vos, I. Bartolozzi, E. Schacht, P. Bienstman, R. Baets, *Opt. Express* **2007**, *15*, 7610.

[4] Y. Chen, H. Lin, J. Hu, M. Li, *ACS Nano* **2014**, *8*, 6955.

[5] B. Jalali, *Nat. Photonics* **2010**, *4*, 506.

[6] M. Sieger, B. Mizaikoff, *Anal. Chem.* **2016**, *88*, 5562.

[7] A. Wilk, J. C. Carter, M. Chrisp, A. M. Manuel, P. Mirkarimi, J. B. Alameda, B. Mizaikoff, *Anal. Chem.* **2013**, *85*, 11205.

[8] R. Soref, *Nat. Photonics* **2010**, *4*, 495.

[9] H. Lin, Z. Luo, T. Gu, L. C. Kimerling, K. Wada, A. Agarwal, J. Hu, *Nanophotonics* **2018**, *7*, 1929.

[10] T. Hu, B. Dong, X. Luo, T.-Y. Liow, J. Song, C. Lee, G.-Q. Lo, *Photonics Res.* **2017**, *5*, 417.

[11] H. A. Atwater, A. Polman, *Nat. Mater.* **2010**, *9*, 205.

[12] J. N. Anker, W. P. Hall, O. Lyandres, N. C. Shah, J. Zhao, R. P. Van Duyne, *Nat. Mater.* **2008**, *7*, 442.

[13] M. Chen, L. Shao, S. V. Kershaw, H. Yu, J. Wang, A. L. Rogach, N. Zhao, *ACS Nano* **2014**, *8*, 8208.

[14] N. Liu, M. Mesch, T. Weiss, M. Hentschel, H. Giessen, *Nano Lett.* **2010**, *10*, 2342.

[15] X. Tang, M. M. Ackerman, P. Guyot-Sionnest, *ACS Nano* **2018**, *12*, 7362.

[16] C. Haffner, W. Heni, Y. Fedoryshyn, J. Niegemann, A. Melikyan, D. L. Elder, B. Baeuerle, Y. Salamin, A. Josten, U. Koch, C. Hoessbacher, F. Ducry, L. Juchli, A. Emboras, D. Hillerkuss, M. Kohl, L. R. Dalton, C. Hafner, J. Leuthold, *Nat. Photonics* **2015**, *9*, 525.

[17] M. Ayata, Y. Fedoryshyn, W. Heni, B. Baeuerle, A. Josten, M. Zahner, U. Koch, Y. Salamin, C. Hoessbacher, C. Haffner, D. L. Elder, L. R. Dalton, J. Leuthold, *Science* **2017**, *358*, 630.

[18] C. Chen, N. Youngblood, R. Peng, D. Yoo, D. A. Mohr, T. W. Johnson, S.-H. Oh, M. Li, *Nano Lett.* **2017**, *17*, 985.

[19] B. Zhu, M. Chen, S. V. Kershaw, A. L. Rogach, N. Zhao, H. K. Tsang, in *2017 Conf. Lasers Electro-Optics Pacific Rim (CLEO-PR)*, IEEE, Piscataway, NJ **2017**, https://doi.org/10.1109/CLEOPR.2017.8118904.

[20] S. Law, V. Podolskiy, D. Wasserman, *Nanophotonics* **2013**, *2*, 103.

[21] A. Rogalski, *Rep. Prog. Phys.* **2005**, *68*, 2267.

[22] B. W. Jia, K. H. Tan, W. K. Loke, S. Wicaksono, S. F. Yoon, *Opt. Express* **2018**, *26*, 7227.

[23] P. Norton, *Opto-Electron. Rev.* **2002**, *10*, 159.

[24] A. Rogalski, *J. Alloys Compd.* **2004**, *371*, 53.

[25] X. Wang, Z. Cheng, K. Xu, H. K. Tsang, J.-B. Xu, *Nat. Photonics* **2013**, *7*, 888.

[26] Q. Guo, A. Pospischil, M. Bhuiyan, H. Jiang, H. Tian, D. Farmer, B. Deng, C. Li, S.-J. Han, H. Wang, Q. Xia, T.-P. Ma, T. Mueller, F. Xia, *Nano Lett.* **2016**, *16*, 4648.

**ADVANCED
SCIENCE NEWS**

www.advancedsciencenews.com

**ADVANCED
MATERIALS
TECHNOLOGIES**

www.advmattechnol.de

[27] M. Long, A. Gao, P. Wang, H. Xia, C. Ott, C. Pan, Y. Fu, E. Liu, X. Chen, W. Lu, T. Nilges, J. Xu, X. Wang, W. Hu, F. Miao, *Sci. Adv.* **2017**, *3*, e1700589.

[28] S. E. Keuleyan, P. Guyot-sionnest, C. Delerue, G. Allan, *ACS Nano* **2014**, *8*, 8676.

[29] S. Keuleyan, E. Lhuillier, V. Brajuskovic, P. Guyot-Sionnest, *Nat. Photonics* **2011**, *5*, 489.

[30] M. M. Ackerman, X. Tang, P. Guyot-sionnest, *ACS Nano* **2018**, *12*, 7264.

[31] M. Chen, H. Lu, N. M. Abdelazim, Y. Zhu, Z. Wang, W. Ren, S. V. Kershaw, A. L. Rogach, N. Zhao, *ACS Nano* **2017**, *11*, 5614.

[32] N. Huo, S. Gupta, G. Konstantatos, *Adv. Mater.* **2017**, *29*, 1606576.

[33] S. Keuleyan, E. Lhuillier, P. Guyot-Sionnest, *J. Am. Chem. Soc.* **2011**, *133*, 16422.

[34] M. V. Kovalenko, E. Kaufmann, D. Pachinger, J. Roither, M. Huber, J. Stangl, G. Hesser, F. Schaffler, W. Heiss, *J. Am. Chem. Soc.* **2006**, *128*, 3516.

[35] N. M. Abdelazim, Q. Zhu, Y. Xiong, Y. Zhu, M. Chen, N. Zhao, S. V. Kershaw, A. L. Rogach, *Chem. Mater.* **2017**, *29*, 7859.

[36] R. Wang, Y. Shang, P. Kanjanaboos, W. Zhou, Z. Ning, E. H. Sargent, *Energy Environ. Sci.* **2016**, *9*, 1130.

[37] G. Konstantatos, E. H. Sargent, *Colloidal Quantum Dot Optoelectronics and Photovoltaics*, Cambridge University Press, Cambridge, UK **2013**.

[38] Z. Cheng, X. Chen, C. Y. Wong, K. Xu, C. K. Y. Fung, Y. M. Chen, H. K. Tsang, *Opt. Lett.* **2012**, *37*, 1217.

[39] B. Q. Zhu, H. K. Tsang, *J. Lightwave Technol.* **2016**, *34*, 2467.

[40] Lumerical Inc., Lumerical MODE Solutions, https://www.lumerical.com/tcad-products/mode/ (accessed: April 2019).

[41] Y. Ding, X. Guan, X. Zhu, H. Hu, S. I. Bozhevolnyi, L. K. Oxenløwe, K. J. Jin, N. A. Mortensen, S. Xiao, *Nanoscale* **2017**, *9*, 15576.

[42] Y. Salamin, P. Ma, A. Emboras, Y. Fedoryshyn, B. Cheng, C. Hafner, J. Leuthold, in *2017 Conf. Lasers Electro-Optics (CLEO)*, IEEE, Piscataway, NJ **2017**, https://doi.org/10.1364/CLEO_SI.2017.STu1N.2.

[43] M. Chen, H. Yu, S. V. Kershaw, H. Xu, S. Gupta, F. Hetsch, A. L. Rogach, N. Zhao, *Adv. Funct. Mater.* **2014**, *24*, 53.

[44] R. H. Bube, *Photoconductivity of Solids*, Wiley, New York, NY **1960**.

[45] H. Liu, E. Lhuillier, P. Guyot-sionnest, *J. Appl. Phys.* **2014**, *115*, 154309.

[46] Y. Lai, H. Li, D. K. Kim, B. T. Diroll, C. B. Murray, C. R. Kagan, *ACS Nano* **2014**, *8*, 9664.

[47] E. L. Dereniak, G. D. Boreman, *Infrared Detectors and Systems*, Wiley, New York, NY **1996**.

1900354 (8 of 8)